J. Fluid Mech. (1971), *vol.* 50, *part* 1, *pp.* 79–95
Printed in Great Britain

Rotating flow over shallow topographies

By ARSALAN VAZIRI AND DON L. BOYER†
Department of Civil Engineering, University of Delaware, Newark, Delaware

(Received 8 April 1971)

The flow of a rotating homogeneous incompressible fluid over various shallow topographies is investigated. In the physical system considered, the rotation axis is vertical while the topography and its mirror image are located on the lower and upper of two horizontal plane surfaces. Upstream of the topographies and outside the Ekman layers on the bounding planes the fluid is in a uniform free-stream motion. An analysis is considered in which $E \ll 1, Ro \sim E^{\frac{1}{2}}, H/D \sim E^{0}$, and $h/D \sim E^{\frac{1}{2}}$, where E is the Ekman number, Ro the Rossby number, H/D the fluid depth to topography width ratio and h/D the topography height-to-width ratio. The governing equation for the lowest-order interior motion is obtained by matching an interior geostrophic region with Ekman boundary layers along the confining surfaces. The equation includes contributions from the non-linear inertial, Ekman suction, and topographic effects. An analytical solution for a cosine-squared topography is given for the case in which the inertial terms are negligible; i.e. $Ro \ll E^{\frac{1}{2}}$. Numerical solutions for the non-linear equations are generated for both cosine-squared and conical topographies. Laboratory experiments are presented which are in good agreement with the theory advanced.

1. Introduction

Since the time of Taylor's (1923) experiments a great deal of effort has been expended in investigating the effects of bottom topography on flows in rotating frames of reference. Unfortunately most of the theoretical studies are so restrictive as to make experimentation difficult, if not impossible, while for many of the experimental studies the theory is intractable. The present investigation is one for which both the range of applicability of the theory and the capabilities of the laboratory experiment coincide.

The physical system to be considered is sketched in figure 1. Identical topographies are mounted in symmetrical pairs on the upper and lower of two infinite horizontal plane surfaces. The region between the bounding surfaces is filled with a homogeneous incompressible fluid and the entire system rotates with a constant angular velocity, $\bar{\omega}$, about a vertical axis. Upstream of the topographies and outside the Ekman layers on the horizontal surfaces the fluid is in a uniform rectilinear motion. The resulting flow field is to be examined.

Jacobs (1964), in a theoretical study, investigated a system similar to that given in figure 1; i.e. he considered only the topography on the lower surface. His analysis is restricted geometrically to obstacles of revolution whose slopes,

† Present address: National Science Foundation, Washington, D.C.

as characterized by h/D, are of order unity everywhere. He obtains a solution in which the motion in the interior of a cylinder circumscribing the obstacle is stagnant while that in the exterior is the classical two-dimensional irrotational flow past a solid cylinder. Vertical shear layers provide the smooth transition between these regions. The analysis neglects inertial effects and as such is very restrictive in that it requires $E \ll 1$ and $Ro \ll E^{\frac{1}{2}}$, where E and Ro are the Ekman and Rossby numbers respectively.

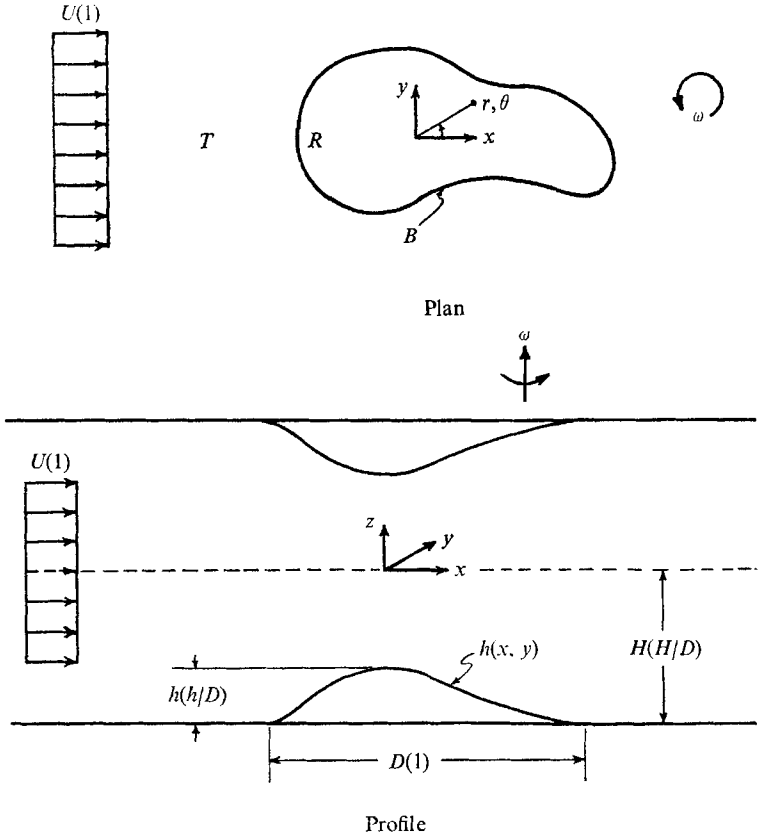

FIGURE 1. The physical system. Quantities in parenthesis are dimensionless.

In another recent analytical study, Ingersoll (1969), using Jacobs' geometry, considered the parameter restrictions $E^{\frac{1}{2}} \ll Ro \ll 1$ and $h/D \sim Ro$; i.e. the analysis, while including inertial effects, neglects viscosity. His analysis predicts, for example, that stagnant columns should occur above right circular cylindrical obstacles whenever $h/D > 2Ro$. These columns are 'partial columns' in the sense that they do not circumscribe the entire obstacle. They occur off-centre (i.e. to the right, facing downstream) for the flow and rotation directions indicated in figure 1. Ingersoll's analysis also predicts a circulation around the column which has the opposite sense to that of the basic rotation. The upstream and downstream flow patterns he obtains are mirror images.

Moore & Saffman (1969) considered the motion of a thin disk through a rotating fluid. Their analysis, which requires $E \ll 1$, $Ro \ll E^{\frac{1}{4}}$ and $h/D \ll E^{\frac{1}{2}}$, and thus

neglects inertial effects, shows that the flow field consists of two geostrophic regions separated by free shear layers in the vicinity of a cylinder circumscribing the disk. The indeterminateness of the geostrophic regions is removed by the constraints imposed by the vertical shear layers. They find that the fluid veers to the right, facing downstream, as it passes over the disk. No stagnant flow regions are obtained.

Hide & Ibbetson (1966) and Hide, Ibbetson & Lighthill (1968) performed various laboratory experiments concerning topography effects on rotating flows. In the former study obstacles were towed through a rotating fluid, i.e. the Taylor experiment. In the latter, a vortex flow was induced in a rotating circular tank by introducing the fluid along the centre-line and removing it along the periphery. The obstacles were then placed in the flow (i.e. fixed with respect to a rotating observer) and the resulting motion was examined.

The present study will employ the rotating water-tunnel described recently by one of us (Boyer 1971*a*). The tunnel can provide a uniform flow with respect to a rotating observer and thus can be used for an experimental investigation of the physical system under consideration (figure 1). To date (Boyer 1970, 1971*a*, *b*) the tunnel has been utilized to investigate the flow past right circular cylinders (extending through the depth of the channel), long ridges (e.g. of triangular cross-section) and a long step (i.e. a ridge of rectangular cross-section), respectively. The cylinder study is purely experimental while the latter investigations are accompanied by theory. The analysis in the ridge and step studies is restricted by the following:

$$E \ll 1, \quad Ro \sim E^{\frac{1}{2}}, \quad h/D \sim E^{\frac{1}{2}}, \quad H/D \sim E^{0}, \tag{1.1}$$

where h/D and H/D are the geometrical parameters defined in figure 1.

In the ridge analysis the topography is assumed to be infinitely long and to have an infinitesimal (i.e. $O(E^{\frac{1}{2}})$) slope everywhere. Thus under conditions (1.1) the resulting flow field is shown to consist of an interior geostrophic region and Ekman layers along the bounding surfaces. While (1.1) ensures that the inertial terms are important, non-linear difficulties do not arise since the two-dimensional aspects of the problem lead to a linearization of these terms. In the step analysis it is shown that free shear layers occur in the vicinity of vertical planes defined by the infinite slope portions of the topography. Since again, however, the topography is assumed to be infinitely long, the problem reduces to a tractable one analytically.

It is the purpose of the present study to investigate the flow over shallow topographies which are finite in extent (e.g. cones) and whose slopes are infinitesimal ($O(E^{\frac{1}{2}})$) everywhere. Topographies, such as disks, which would be accompanied by free vertical shear layers are not considered. Restrictions (1.1) are retained and thus the problem posed is general, in the sense that the inertial, Coriolis, topographic, and viscous effects are all important in determining the lowest-order motion. It is recognized at the outset that the non-linear inertial terms must be considered in the analysis. As such, solutions are obtained using numerical techniques. The experimental objective is to generate laboratory flows which can be compared with some of the numerical results.

2. Formulation

The dimensionless equations of motion for a homogeneous incompressible fluid relative to a rectangular Cartesian co-ordinate system $\mathbf{x}(x, y, z) = \mathbf{x}^*/D$ rotating at a constant angular velocity $\omega\hat{\mathbf{k}}$ with respect to an inertial frame are

$$Ro[\mathbf{v}_t + (\mathbf{v}.\nabla)\,\mathbf{v}] = -\nabla\Phi - \hat{\mathbf{k}} \times \mathbf{v} + E\nabla^2\mathbf{v}, \tag{2.1}$$

where D is the characteristic horizontal dimension of the topography, $Ro = U/2\omega D$ the Rossby number, U the free-stream speed, $\mathbf{v}(u, v, w) = \mathbf{v}^*/U$ the Eulerian velocity, $t = t^*U/D$ the time, $\Phi = (-\frac{1}{2}\omega^2 c^2 + p/\rho + \phi)/2\omega UD$, c the distance from the axis of rotation, p the pressure, ρ the density, ϕ the gravitational potential, $E = \nu/2\omega D^2$ the Ekman number, and ν the kinematic viscosity. The asterisks refer to dimensional quantities. The equation for conservation of mass is given by

$$\nabla.\mathbf{v} = 0. \tag{2.2}$$

We apply no-slip boundary conditions on the confining surfaces and require that the flow outside of the Ekman layers is uniform far upstream and at large lateral distances from the topography. Far downstream we require the streamlines to be parallel to their upstream directions.

From (2.1) and (2.2) and the attendant boundary conditions for the symmetric system being considered it is clear that u, v and Φ are even in the vertical co-ordinate, z, while w is odd in z. We thus need consider only the region $z \leqslant 0$.

The problem posed is a four-parameter one including Ro and E, which appear in the governing equations, and h/D and H/D, defined in figure 1, which enter through the boundary conditions. The general problem is intractable analytically and one is thus led to make simplifying approximations.

We consider the following *a priori* assumptions: (i) $E \ll 1$; (ii) $Ro = kE^{\frac{1}{2}}$, where k is of order unity; (iii) $H/D \sim E^0$, i.e. of order unity; (iv) $h/D \sim E^{\frac{1}{2}}$, let the bottom topography be given by

$$z = -H/D + E^{\frac{1}{2}}h_0(x, y), \quad \text{where} \quad h_0(x, y) = E^{-\frac{1}{2}}h(x, y)/D \sim E^0;$$

(v) $h_{0x} \sim E^0$, $h_{0y} \sim E^0$, i.e. the topography slope is infinitesimal everywhere. These assumptions ensure that inertial, Coriolis, topographic and viscous effects will all be important in the determination of the lowest-order motion.

Since the formulation here is similar to that discussed by both Ingersoll (1969) and Boyer (1971*a*), a detailed derivation of the simplified governing equations will be omitted. For details of this derivation or of other portions of this paper, the reader is referred to Vaziri (1971). Very briefly, however, under restrictions (i) to (v) the flow field can be divided into an interior geostrophic region and Ekman layers along the bounding surfaces. In each of these regions the dependent variables can be expanded in power series in $E^{\frac{1}{2}}$.

The zeroth-order motion (i.e. of order unity) in the interior is geostrophic and horizontal. It is not possible, however, to determine the geostrophic flow field unless the first-order (i.e. $O(E^{\frac{1}{2}})$) interior terms are also considered. The first-order equations provide a relation between the lowest-order non-zero vertical

velocity component, W_I, (i.e. $O(E^{\frac{1}{2}})$) and the zeroth-order horizontal motion One obtains, to lowest order,

$$W_I = kz\{\xi_t + J(\psi, \xi)\} E^{\frac{1}{2}}, \tag{2.3}$$

where ξ is the vertical component of relative vorticity and ψ is the stream function. Here ψ is defined by $U_0 = -\psi_y$ and $V_0 = \psi_x$, where U_0, V_0 are the zeroth-order horizontal interior velocity components. The stream function and relative vorticity are related by the Poisson equation

$$\nabla^2 \psi = \xi. \tag{2.4}$$

It should be noted that steady solutions are sought, but because of the numerical techniques employed, the unsteady terms have been retained.

From an analysis of the Ekman layers, the leading-order vertical velocity component W_E, evaluated at the outer edges of the boundary layers, is given by

$$W_E = \{2^{-\frac{1}{2}}\xi + J(\psi, h_0)\} E^{\frac{1}{2}}. \tag{2.5}$$

Matching the interior (2.3) and the Ekman layers (2.5) along the lower boundary, $z = -H/D$ to lowest order, yields

$$k(H/D)\{\xi_t + J(\psi, \xi)\} + 2^{-\frac{1}{2}}\xi + J(\psi, h_0) = 0, \tag{2.6}$$

where terms of $O(E^{\frac{1}{2}})$ (or $O(Ro)$) have been neglected. Equations (2.4) and (2.6) are to be solved for the interior values of ψ and ξ.

Relation (2.6) is a transport equation for the relative vorticity. The terms in (2.6) are respectively the unsteady, advection, Ekman suction (pumping) and topographical contributions. The boundary conditions require

$$\left.\begin{aligned} \psi(x \to -\infty, y) &= -y, \\ \psi(x, y \to \pm\infty) &= \mp y, \\ \psi_x(x \to \infty, y) &= 0. \end{aligned}\right\} \tag{2.7a,b,c}$$

In order to obtain solutions the topography is specified in a region R as projected on the x, y plane (figure 1). In the region T, outside R, the bounding planes are horizontal and hence the topography terms are identically zero. Let the boundary between R and T be specified as B. In obtaining solutions one solves (2.4) and (2.6) in R and T and matches the solutions along B. The matching requires that both the velocity and shear stress be continuous.

For topographies with continuous slopes everywhere no apparent difficulties will arise since the problem, as formulated, will yield lowest-order interior and Ekman layer solutions which are continuous and which satisfy the requisite boundary conditions. Special care must be exercised, however, when the topography in question has discontinuities in slope. Consider, for example, a topography for which there is a slope discontinuity along B (e.g. a cone). It is clear from (2.4) and (2.6) and the stated continuity conditions on the velocity and shear stress that ψ_{nnn} will, in general, not be continuous across B; here n is the derivative taken normal to B. From (2.3), discontinuities in ψ_{nnn} imply discontinuities in the lowest-order interior vertical velocity component. Thus while the zeroth-order horizontal velocity components will be continuous, the vertical component will be discontinuous along B.

Consider a hypothetical 'smoothing process' in which the topography slope is made continuous over a horizontal distance of $O(E^{\lambda})$ normal to B. We restrict to $\lambda < \frac{1}{2}$ so that the first-order z-momentum equation is hydrostatic as required in the derivation of (2.6). If we further require $\lambda > 0$, the lowest-order horizontal motion, as determined from (2.4) and (2.6), for the smoothed and the discontinuous slope topographies will be identical since the smoothing has not altered the lowest-order topography. Such a smoothing thus provides a continuous lowest-order vertical velocity field without altering the lowest-order horizontal motion. Since we are interested mainly in the horizontal velocity field, the details of the smoothing process need not be considered.

In the next section the non-linear advection terms are neglected and a solution for the resulting linear problem is sought. Under these conditions it is not possible to obtain horizontal flow fields for which both the velocity and shear stress are continuous unless one restricts to topographies with continuous slopes everywhere. If the inertial terms are neglected a discontinuity in slope would presumably be accompanied by vertical shear layers. Since we do not wish to address such layers in the present paper, we restrict to topographies with continuous slopes in considering the linear problem.

3. Linear problem

In order to emphasize the importance of non-linear effects, the linear problem will first be investigated. We omit the unsteady term in (2.6) and also assume that the inertial terms are negligible; i.e. $Ro \ll E^{\frac{1}{2}}$. Combining (2.4) and (2.6), the governing equation for ψ in polar co-ordinates is thus given by

$$\nabla^2\psi + (2^{\frac{1}{2}}/r)\,(\psi_r h_{0\theta} - \psi_\theta h_{0r}) = 0. \tag{3.1}$$

Consider as an example a cosine-squared topography defined by

$$h_0(r) = \begin{cases} E^{-\frac{1}{2}}(h/D)\cos^2\pi r, & r \leqslant \frac{1}{2}, \quad \text{region } R \\ 0, & r > \frac{1}{2}, \quad \text{region } T \end{cases} \tag{3.2}$$

where $h/D \sim O(E^{\frac{1}{2}})$ is the dimensionless amplitude. Both the topography and its slope are continuous throughout the entire domain. From (3.1) and (3.2) the equations for the stream function in regions R and T are given by

$$\nabla^2\psi_R = -2^{\frac{3}{2}}\pi E^{\frac{1}{2}}(h/D)\,(1/r)\sin\pi r\cos\pi r \tag{3.3}$$

and

$$\nabla^2\psi_T = 0, \tag{3.4}$$

respectively. The boundary conditions require

$$\left.\begin{aligned} \psi_R(\tfrac{1}{2},\theta) &= \psi_T(\tfrac{1}{2},\theta), \\ \psi_{Rr}(\tfrac{1}{2},\theta) &= \psi_{Tr}(\tfrac{1}{2},\theta), \\ \psi_T(r\to\infty,\theta) &= -r\sin\theta. \end{aligned}\right\} \tag{3.5}$$

The solution of (3.3) and (3.4) subject to (3.5) is straightforward but lengthy. The series solution of (3.4) is standard while that of (3.3) is obtained by the method of Frobenius. The details of the solution are given in Vaziri (1971) and will not be repeated here.

A typical streamline pattern is shown in figure 2. In this and all subsequent figures the flow is from left to right, the rotation is counterclockwise, and the topography is indicated by dashed lines. One of the apparent features of the flow is its symmetry in the sense that $\psi(r,\theta) = -\psi(r,\theta+\pi)$. Note also that the characteristic speed near the central portion of the topography is relatively small as indicated by the large separation distance between streamlines.

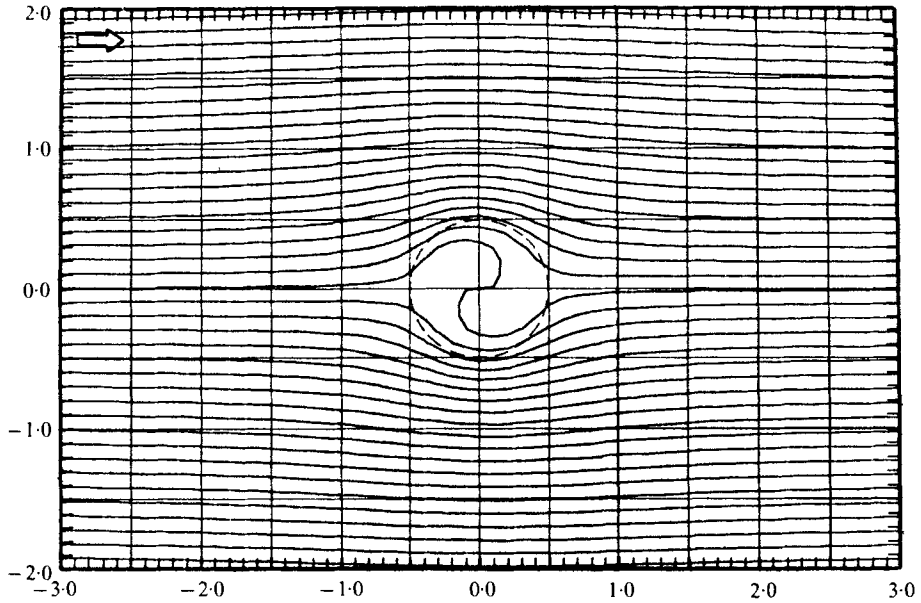

FIGURE 2. Streamline patterns for a cosine-squared topography, $E = 2{\cdot}6 \times 10^{-4}$ and $h/D = 6{\cdot}25 \times 10^{-2}$. Here and in all streamline patterns to follow, the flow is from left to right, the rotation is counterclockwise and the increment between adjacent streamlines is 0·2.

4. Non-linear problem – numerical techniques

Steady-state solutions for ψ and ξ for (2.4) and (2.6) subject to the boundary conditions (2.7) can be obtained numerically using a procedure similar to that given in a classical paper by Charney, Fjörtoft & von Neumann (1950) and used extensively in numerical treatments of oceanographical and meteorological problems. The integration is performed in a rectangular domain X, Y sketched in figure 3. Let the domain be subdivided into a network of M, N grid points in the x and y directions, respectively. For convenience the grid interval d is chosen the same size in both directions, i.e.

$$d = \frac{X}{M-1} = \frac{Y}{N-1}.$$

The time increment is Δt, so that $t = n\Delta t$, where $n = 0, 1, 2, \ldots$.

We define the value of $\psi(x,y,t)$ at the grid point (i, j) and time $n\Delta t$ as $\psi^n_{i,j}$.

Derivatives are written in finite difference form using a centred difference scheme, i.e.

$$\frac{\partial \psi}{\partial x} = \frac{\psi^n_{i+1,j} - \psi^n_{i-1,j}}{2d} + O(d^2),$$

$$\frac{\partial \psi}{\partial y} = \frac{\psi^n_{i,j+1} - \psi^n_{i,j-1}}{2d} + O(d^2),$$

$$\frac{\partial \psi}{\partial t} = \frac{\psi^{n+1}_{i,j} - \psi^{n-1}_{i,j}}{2\Delta t} + O(\Delta t^2).$$

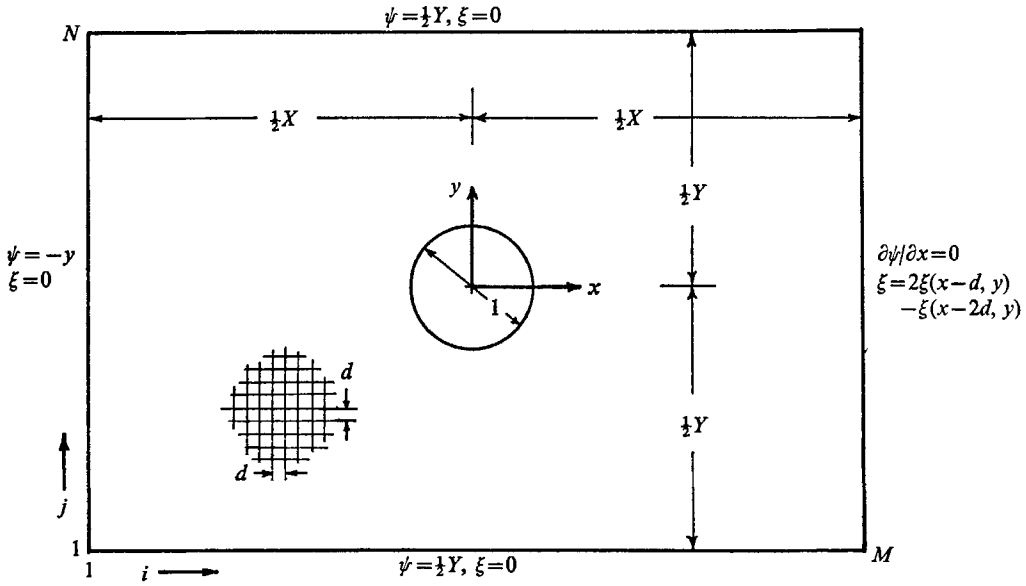

FIGURE 3. Integration domain and boundary conditions for the numerical calculations.

With these definitions, the finite difference analogues of (2.6) and (2.4) can be written as

$$\xi^{n+1}_{i,j} = \frac{1-a\Delta t}{1+a\Delta t}\xi^{n-1}_{i,j} + \frac{\Delta t}{1+a\Delta t}\left\{2J(\xi^n, \psi^n) + \frac{b}{d}[(h_{0x})_{i,j}(\psi^n_{i,j+1} - \psi^n_{i,j-1}) - (h_{0y})_{i,j}(\psi^n_{i+1,j} - \psi^n_{i-1,j})]\right\}, \quad (4.1)$$

$$(1/d^2)(\psi^n_{i+1,j} + \psi^n_{i-1,j} + \psi^n_{i,j+1} + \psi^n_{i,j-1} - 4\psi^n_{i,j}) = \xi^n_{i,j}, \quad (4.2)$$

respectively, where the Ekman suction term, $a\xi$, has been approximated by $\frac{1}{2}a(\xi^{n+1}_{i,j} + \xi^{n-1}_{i,j})$, and $J(\xi^n, \psi^n)$ is the finite difference form of the Jacobian due to Arakawa (1966). The Jacobian and topography terms are evaluated at the central time level n. Predicted values of vorticity $\xi^{n+1}_{i,j}$ are obtained at time level $n+1$ according to (4.1). The stream-function field $\psi^n_{i,j}$ is determined from a solution of the Poisson equation (4.2). The truncation errors in (4.1) and (4.2) are $O(d^2)$ or $O(\Delta t^2)$. At $t = 0$ the flow is assumed to be uniform throughout the domain and, from (4.2), the vorticity is thus zero everywhere, i.e.

$$\psi(t = 0) = -y, \quad \xi(t = 0) = 0.$$

At $t > 0$ the boundary conditions on ψ are given by (2.7). In order to solve the prediction equation (4.1) boundary conditions on vorticity must also be specified. By combining the Poisson equation (4.2) with (2.7*a*, *b*) the boundary conditions on the vorticity for the inflow and two lateral boundaries are given by

$$\xi(x = -\tfrac{1}{2}X) = 0, \quad \xi(y = \pm\tfrac{1}{2}Y) = 0,$$

respectively. On the outflow boundary, $x = \frac{1}{2}X$, the stream function is unknown and the vorticity may be determined from the interior values through a simple extrapolation proposed by Charney *et al.*, i.e.

$$\xi(x = \tfrac{1}{2}X - d) - \xi(x = \tfrac{1}{2}X - 2d) = \xi(x = \tfrac{1}{2}X) - \xi(x = \tfrac{1}{2}X - d).$$

The scheme used for the numerical integration of (4.1) and (4.2) is now standard. The complete algorithm consists of predicting vorticity $\xi_{i,j}^{n+1}$ according to (4.1), except for an initial forward time step. Knowing the vorticity distribution, the Poisson equation (4.2) is then solved for the stream function. The procedure is repeated until the solutions converge, e.g. they satisfy the relation

$$\frac{\left|\sum_{i,j}(\xi_{i,j}^{n})^2 - \sum_{i,j}(\xi_{i,j}^{n-m})^2\right|}{\sum_{i,j}(\xi_{i,j}^{n})^2} < \epsilon, \tag{4.3}$$

where m is an even number and ϵ is an acceptable tolerance.

One of the serious questions to be considered in any numerical integration is that of stability. There is a great deal of analytical and numerical work in the literature concerned with the stability properties of various time and space differencing techniques. These fundamentals will not be discussed here. Instead, the methods employed to neutralize possible computational instabilities are briefly reviewed. For a more detailed discussion, see Williams (1969).

The advection process has a well-known partial instability (see, for example, Richtmyer & Morton 1957, Forsythe & Wasow 1960) which can be suppressed by realizing the Courant–Friedrichs–Lewy criterion that the time step be limited to $\Delta t \leqslant d/2^{\frac{1}{2}} \max(\nabla\psi)$.

The limitation on the time step alone does not ensure the stability of the non-linear equation (4.1) and computations may eventually become unstable due to 'aliasing errors' (Phillips 1959). This instability arises after numerous time steps and is caused by the misrepresentation of the shorter waves due to the inability of the finite grid size to properly resolve them. Arakawa (1966) has shown, however, that the non-linear instability can be avoided by proper space differencing of the Jacobian. Using Arakawa's Jacobian, which conserves some of the physical quantities of the flow (i.e. the mean kinetic energy $\overline{\frac{1}{2}(\nabla\psi)^2}$, mean-square vorticity $\overline{\xi^2}$, and the mean vorticity $\overline{\zeta}$, of the system), the aliasing errors may be controlled and the non-linear instability does not occur.

The weak instability associated with the centred time differencing of the unsteady term $\partial\xi/\partial t$ is usually referred to as 'time splitting', e.g. Lilly (1965). This is caused by the fact that a first-order continuous equation, such as (2.6), has been raised to a second-order difference equation, (4.1), involving three time levels. As computations proceed in time, two modes of solutions develop: one associated with the physical solution and one a purely 'computational mode'

arising from the method of time integration (Platzman 1954). If the weak instability can be kept small, the centred time differencing, being an accurate one, is desirable. The weak instabilities can be kept small by periodically taking a forward time step in the calculations and then continuing the integration with the centred time differencing, (4.1).

The instability of the Ekman suction term $a\xi$, in a vorticity equation of the form $\xi_t = a\xi$, has been examined by Miyakoda (1962). With $a > 0$ and centred time differencing, the scheme is unstable if ξ is evaluated at the central time level n. A stable scheme is obtained, however, if ξ is approximated by its average value at the non-centred time levels, i.e. $\xi = (\xi_{i,j}^{n+1} + \xi_{i,j}^{n-1})/2\Delta t$.

The instability properties of the topographical terms are not considered here since these terms are identically zero over the major part of the domain.

At every time step the Poisson equation (4.2) has to be solved for the stream function ψ. While there are numerous solution techniques available, care must be taken to choose a method which is both accurate and relatively rapid. The fastest iterative method presently available for a rectangular domain and subject to mixed boundary conditions is the alternating-direction implicit (ADI) method which is described in detail by Varga (1962) and Wachspress (1966). Using the ADI scheme, the Poisson equation can be solved very accurately in an average of less than 1 sec on a CDC 6600 machine for a 61×41 rectangular domain with mixed boundary conditions (2.7).

5. Numerical results

We first obtain solutions for the cosine-squared topography defined by (3.2). The parameters E and h/D are taken to be the same as those used in obtaining the flow pattern for the linear problem (figure 2) while Ro is now made finite. The resulting streamline and vorticity fields are given in figures 4(*a*) and 4(*b*) respectively. As should be expected, the symmetry of the flow pattern as noted in the zero Rossby number calculation (figure 2) is destroyed when Ro is non-zero, figure 4(*a*). One also notes, in comparing figures 2 and 4(*a*), that the characteristic speed over the topography is much larger when the Rossby number is finite. The streamlines near the centre of the domain in the non-linear flow experience a net shift to the right, facing downstream, of their upstream positions. This can be observed by tracing a streamline from the inflow to the outflow boundaries. Such a shift is absent in the linear solution.

The corresponding vorticity distribution is shown in figure 4(*b*). The most apparent characteristics of the vorticity distribution are the two cells of opposing signs located in the vicinity of the obstacle. The negative cell appears near the centre of the topography while the positive one is off-centre further downstream. The contours corresponding to $\xi = 0$ have been suppressed for clarity. Since the vorticity is proportional to the Ekman suction velocity, there is a suction of fluid into the Ekman layers in the negative cell and a pumping into the interior in the positive one. We recall that this suction and pumping imply a downward and upward motion respectively throughout the interior in these regions. Note also that the vorticity is advected downstream in an asymmetric fashion.

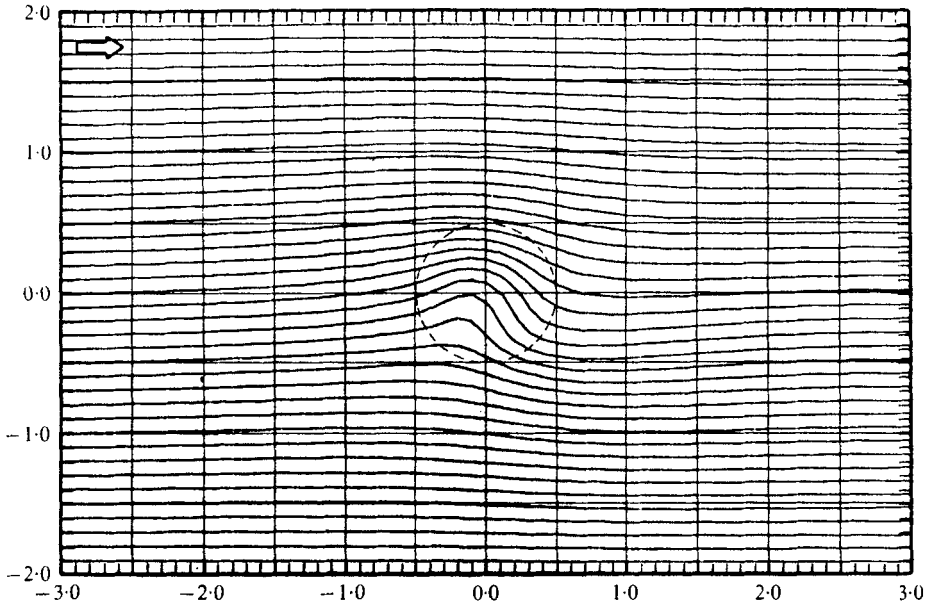

(*a*)

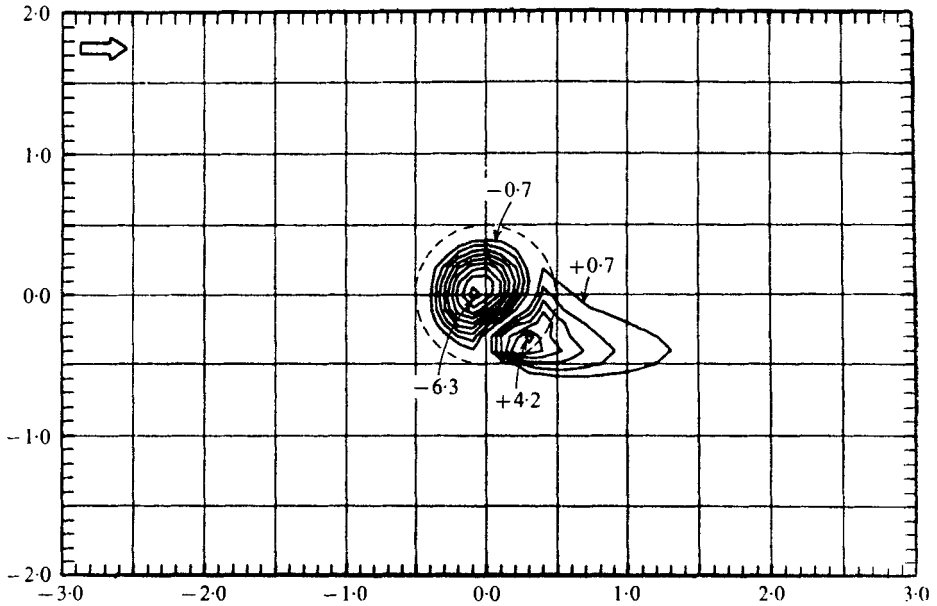

(*b*)

FIGURE 4. (*a*) Streamline patterns for a cosine-squared topography, $E = 2{\cdot}6 \times 10^{-4}$, $Ro = 1{\cdot}8 \times 10^{-2}$, $H/D = 0{\cdot}375$ and $h/D = 6{\cdot}25 \times 10^{-2}$. (*b*) Vorticity distribution; the contour interval is 0·7 and the zero contour lines have been suppressed for clarity.

Because of the difficulties inherent in fabricating topographies as complex as the cosine-squared one, most of the numerical runs were made for a conical topography defined by

$$h_0 = \begin{cases} E^{-\frac{1}{2}}(h/D)\,[1-2(x^2+y^2)^{\frac{1}{2}}], & (x^2+y^2)^{\frac{1}{2}} \leqslant \frac{1}{2}, \\ 0, & (x^2+y^2)^{\frac{1}{2}} \geqslant \frac{1}{2}, \end{cases} \tag{5.1}$$

where h/D is the dimensionless height of the cone.

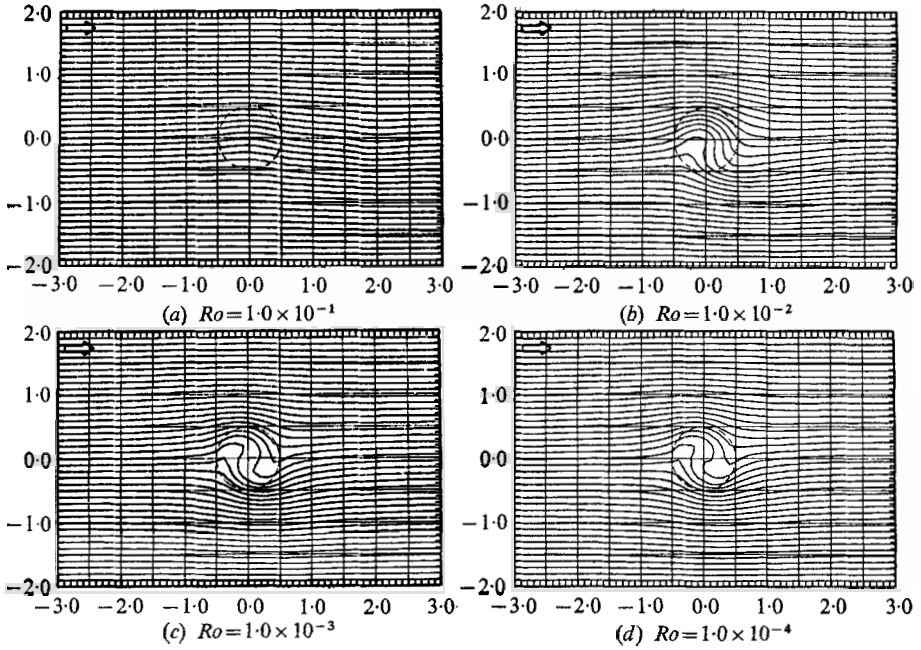

FIGURE 5. Streamline patterns for a conical topography at fixed E, H/D and h/D, and varying Ro. $E = 1{\cdot}0 \times 10^{-4}$, $H/D = 0{\cdot}375$ and $h/D = 6{\cdot}25 \times 10^{-2}$.

Before comparing some of these runs with experiment, we intend to demonstrate how parameter variations alter the resulting flow field. We first note that while the general problem posed is a four-parameter one, the horizontal motion in the simplified problem, as defined by (2.4) and (2.6) and the attendant boundary conditions (2.7), is characterized by only two parameters, i.e. $RoE^{-\frac{1}{2}}(H/D)$ and $E^{-\frac{1}{2}}h/D$. In the following, however, we will examine the behaviour of the horizontal flow field under variations in Ro, E and h/D, since these are the parameters usually varied in the laboratory; $H/D = 0{\cdot}375$ is not varied. Three sets of streamline patterns are presented. In each of these sets one of the parameters Ro, E and h/D is varied while the remaining ones are held fixed. Note that variations in Ro for fixed E and h/D could also be considered as a variation in H/D for fixed Ro, E and h/D.

The streamline patterns for various Ro and fixed E and h/D are shown in figure 5. The most apparent characteristic of decreasing Ro is that of increased streamline deflexions above the obstacle. It is also clear that the characteristic fluid velocities above the cone decrease with decreasing Ro. Finally, note that as Ro is made

smaller, the flow patterns become more symmetrical in the sense of the linear problem as exemplified by figure 2. This should be expected since the inertial effects become less important as Ro is decreased.

Streamline patterns for various Ekman numbers and fixed Ro and h/D are given in figure 6. The most striking feature of this series is the development of a bound eddy as the Ekman number is decreased. The eddy is a volume of fluid with a low characteristic speed and is not penetrated by the interior flow. Note

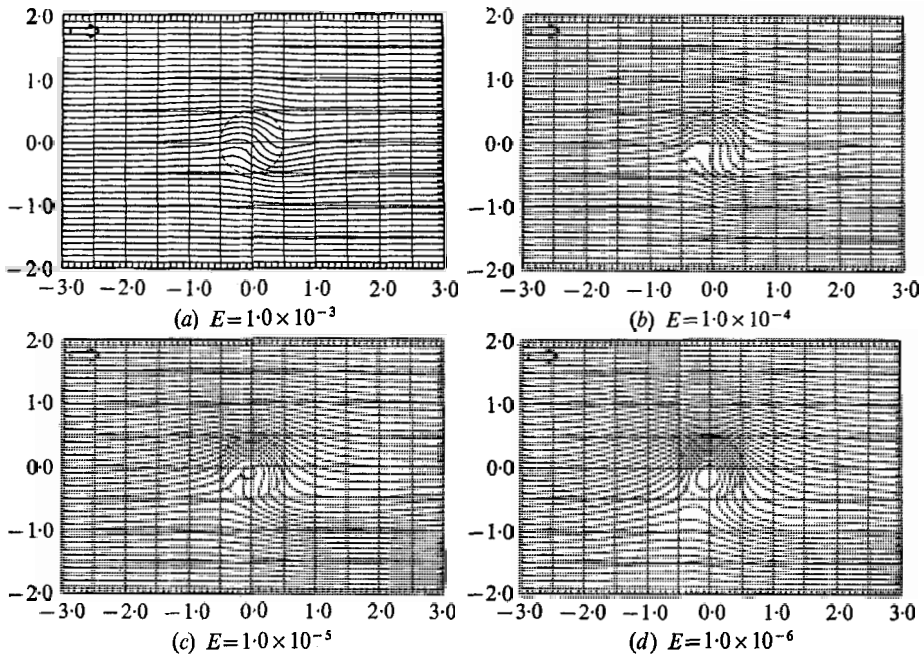

FIGURE 6. Streamline patterns for a conical topography at fixed Ro, H/D and h/D, and varying E. $Ro = 1{\cdot}0\times10^{-2}$, $H/D = 0{\cdot}375$ and $h/D = 6{\cdot}25\times10^{-2}$.

that in figure 6(*d*), Ingersoll's inviscid assumption, $Ro \gg E^{\frac{1}{2}}$, is closely approximated. The gross features of the flow are quite similar to those he obtained even though his computation was for a right circular cylindrical obstacle. Note that the fluid velocities above and on the left-hand side of the cone, facing downstream, are larger than those in the free stream.

Flow fields for increasing cone height h/D and fixed Ro and E are shown in figure 7. Note that the larger h/D runs do not rigorously satisfy the assumption of $h/D \sim E^{\frac{1}{2}}$. Experimental studies, presented below, suggest that the theory, although derived for infinitesimal topographies, can be utilized to a good approximation for finite ones as well.

As seen in figure 7, the general result of increasing h/D is to produce larger streamline deflexions and smaller characteristic fluid velocities above the cone. Note that the $\psi = 0$ streamline in figure 7(*c*) 'curls' through 315° over the cone before continuing downstream. In figure 7(*d*) the apexes of the cones on the top and bottom planes 'just touch'. In this case another bound eddy occurs.

In contrast to those in figure 6, however, this one occurs on the left-hand side of the cone facing downstream. The kinks in the streamlines in figures 7(*c*) and (*d*) are due to the relatively large grid size used in the computations.

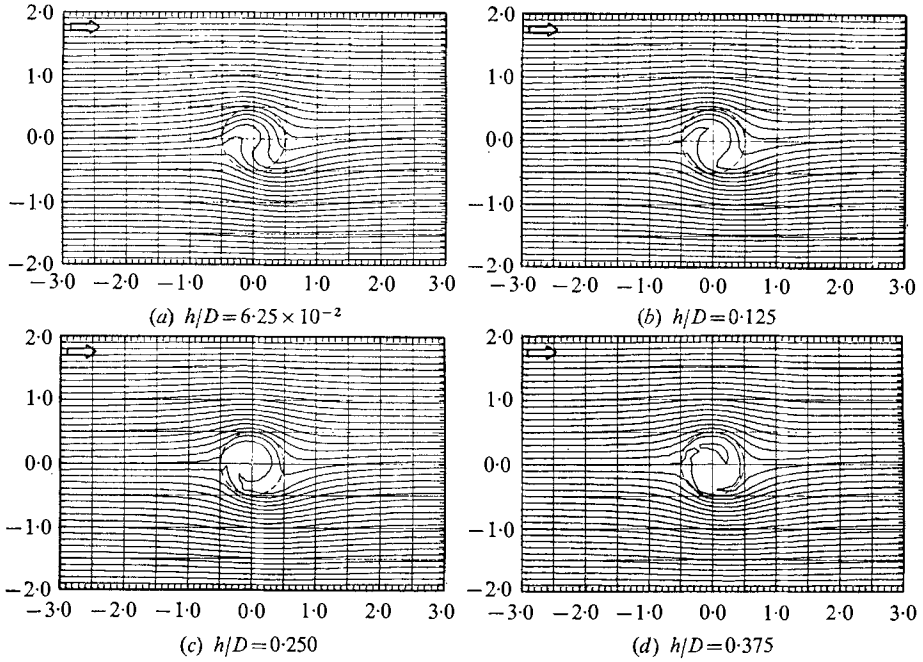

FIGURE 7. Streamline patterns for a conical topography at fixed Ro, E and H/D, and varying h/D; $Ro = 0{\cdot}6 \times 10^{-2}$, $E = 0{\cdot}8 \times 10^{-4}$ and $H/D = 0{\cdot}375$.

6. Experimental studies

The numerical results can be compared with experiment by utilizing the rotating water-tunnel apparatus discussed in some detail by Boyer (1971*a*). Very briefly, the tunnel is a channel of rectangular cross-section (115 cm long, 35 cm wide and 3·8 cm deep). Water is pumped through the channel and the entire system rotates counterclockwise at a constant angular velocity about a vertical axis. By properly adjusting the entrance and exit conditions, the tunnel can provide a test section flow which is uniform outside the Ekman layers on the horizontal plane surfaces.

The uniform flow is at a slight angle (i.e. a few degrees), θ, to the right of the channel axis as one faces downstream. This angle can be computed by balancing the Ekman transport with the cross-channel interior flow. One obtains

$$\tan\theta = (1/2H)\,(\nu/\omega)^{\frac{1}{2}}.$$

Within experimental error this relation is satisfied in the laboratory.

The experiments in the present study are to investigate the interior geostrophic region. A tracer is released from a series of equally spaced lateral positions in the midplane ($z = 0$) of the tunnel and upstream of the topographies. Since the vertical velocity in the midplane is zero, the streaklines so formed depict the streamlines in that plane. Since the lowest-order motion is geostrophic, these

streamlines are representative of the horizontal motion throughout the depth of the fluid.

With the present experimental apparatus it is not possible to obtain the combination of slow enough free-stream flows and large enough rotation rates so that the linear theory is applicable, i.e. so that $Ro \ll E^{\frac{1}{2}}$. It is possible, however, to experiment in the range of applicability of the non-linear theory, i.e. $Ro \sim E^{\frac{1}{2}}$. Figures 8 and 9 (plates 1 and 2) are photographs of experimental runs for a conical topography in which the requirements of the theory are seemingly met. The corresponding numerical solutions are included for comparison.

The photographs are taken from above with the camera facing vertically downward. The cone attached to the upper bounding surface is transparent while the one on the lower surface is fabricated from white Plexiglas in order to provide a good background for photography. The cone system is the dark circular region in the central portion of the photographs and the grid spacing is 2·54 cm. The lateral walls of the tunnel are approximately 17·5 cm from the centre of the obstacle. The flow patterns are apparently unaffected by these side walls. The flow direction is from left to right and the rotation is counterclockwise.

Note, as discussed above, that the upstream flow on average is at a slight angle to the channel axis. The free-stream flow in the numerical runs on the other hand is parallel to the grid lines. Thus one must rotate the experimental runs slightly in order to compare them with the numerical results. This correction is minor, however, and is ignored in the following. Owing to experimental difficulties, the streamline spacing is not identical to that in the numerical runs. Note also that the experimental spacing is not uniform.

With the above in mind it is evident from both figures 8 and 9 that there is good agreement between theory and experiment. Specifically one should note the following. (i) In the upper portions of an imaginary cylinder circumscribing the cone, the fluid velocities are larger than those occurring in the free stream. In the lower regions, expecially in the third quadrant, the velocities are smaller than the free stream. (ii) Fluid is transported in an asymmetric fashion through the circumscribing cylinder; i.e. more fluid enters through that portion of the cylinder in the second quadrant than does through the third, while correspondingly more leaves through the fourth than through the first. (iii) The rightward shift, facing downstream, in the lateral positions of the streamlines passing over the cone is noted in both the experiments and the numerical runs. The experimental shifts, however, are slightly larger than those predicted by the numerical solutions. (iv) One quantitative comparison that can be made is that of the predicted, V_N, and measured, V_E, average speed through an imaginary circumscribing cylinder. By definition, V is the dimensionless upstream separation distance between the two outermost streamlines tangent to the cylinder. From figures 8 and 9 one obtains

$$V_E = 0{\cdot}96 \pm 0{\cdot}03, \quad V_N = 0{\cdot}97 \quad \text{(figure 8)},$$
$$V_E = 0{\cdot}81 \pm 0{\cdot}03, \quad V_N = 0{\cdot}81 \quad \text{(figure 9)},$$

respectively. Thus the quantitative agreement, at least in this respect, is quite good.

One should recall that the lowest-order theory contains errors of the order of the Rossby number. This may account for some of the minor discrepancies between theory and experiment noted in figures 8 and 9. It should also be emphasized that the various experimental errors, as, for example, shear in the free-stream flow, improper entrance and exit conditions, inaccuracies in fabrication and mounting of the models, observational errors, and non-neutrally-buoyant tracer effects may also lead to discrepancies.

Another series of experiments was conducted using a conical obstacle of large slope, i.e. one for which $h/D \sim E^0$. Although the theory is limited to shallow topographies (i.e. $h/D \sim E^{\frac{1}{2}}$), the purpose here was to determine whether the theory will give reasonable predictions for topographies of large slope. As an example, an experimental streamline pattern and the corresponding numerical run for such a topography are shown in figure 10 (plate 3). Quite obviously, these flow patterns agree quite well, and exhibit the same qualitative characteristics as those just delineated. The corresponding average speeds are given by $V_E = 0{\cdot}70 \pm 0{\cdot}03$ and $V_N = 0{\cdot}79$. Thus the average speed predicted numerically is about 13% larger than that obtained experimentally. That there is some quantitative disagreement should of course be expected since the parameter restrictions of the theory are not rigorously met. Nevertheless, the overall agreement suggests that the theory may be satisfactorily extended to finite amplitude topographies.

This research was supported by the Atmospheric Sciences Section, Division of Environmental Sciences of the National Science Foundation under grants GR-943 and GA-24650. Acknowledgment is made to the National Center for Atmospheric Research, which is sponsored by the National Science Foundation, for use of its Control Data 6600 computer.

REFERENCES

ARAKAWA, A. 1966 Computational design for long-term numerical integration of the equations of fluid motions: two-dimensional flow. Part 1. *J. Comput. Phys.* **1**, 119.

BOYER, D. L. 1970 Flow past a right circular cylinder in a rotating frame. *J. Basic Eng. A.S.M.E.* D**92**, 430.

BOYER, D. L. 1971*a* Rotating flow over long shallow ridges. *J. Geophys. Fluid Dynamics*, **2**, 165.

BOYER, D. L. 1971*b* Rotating flow over a step. *J. Fluid Mech.* to be published.

CHARNEY, J. G., FJÖRTOFT, R. & VON NEUMANN, J. 1950 Numerical integration of the barotropic vorticity equation. *Tellus*, **2**, 237.

FORSYTHE, G. E. & WASOW, W. R. 1960 *Finite-Difference Methods for Partial-Differential Equations*. John Wiley.

HIDE, R. & IBBETSON, A. 1966 An experimental study of Taylor columns. *Icarus*, **5**, 279.

HIDE, R., IBBETSON, A. & LIGHTHILL, M. J. 1968 On slow transverse flow past obstacles in a rapidly rotating fluid. *J. Fluid Mech.* **32**, 251.

INGERSOLL, A. P. 1969 Inertial Taylor columns and Jupiter's Great Red Spot. *J. Atmos. Sci.* **26**, 744.

JACOBS, S. J. 1964 The Taylor column problem. *J. Fluid Mech.* **20**, 581.

LILLY, D. K. 1965 On the computational stability of numerical solutions of time-dependent non-linear geophysical fluid dynamics problems. *Mon. Weather Rev.* **93**, 11.

MIYAKODA, K. 1962 Contribution to the numerical weather prediction-computation with finite difference. *Jap. J. Geophys.* **3**, 75.

MOORE, D. W. & SAFFMAN, P. G. 1969 Flow induced by the transverse motion of a thin disk in its own plane through a contained rapidly rotating viscous liquid. *J. Fluid Mech.* **39**, 831.

PHILLIPS, N. A. 1959 An example of non-linear computational instability. In *The Atmosphere and Sea in Motion*. Rockefeller Institute Press.

PLATZMAN, G. W. 1954 The computational stability of boundary conditions in numerical integration of the vorticity equation. *Arch. Met. Geophys. Bioklim.* A**7**, 29.

RICHTMYER, R. D. & MORTON, K. W. 1957 *Difference Methods for Initial Value Problems*. Interscience.

TAYLOR, G. I. 1923 Experiments on the motion of solid bodies in rotating fluids. *Proc. Roy. Soc.* A **104**, 213.

VARGA, R. S. 1962 *Matrix Iterative Analysis*. Prentice Hall.

VAZIRI, A. 1971 Rotating flow over shallow topographies. Ph.D. dissertation. Department of Civil Engineering, University of Delaware.

WACHSPRESS, E. 1966 *Iterative Solution of Elliptic Systems*. Prentice Hall.

WILLIAMS, G. P. 1969 Numerical integration of the three-dimensional Navier-Stokes equations for incompressible flow. *J. Fluid Mech.* **37**, 727.

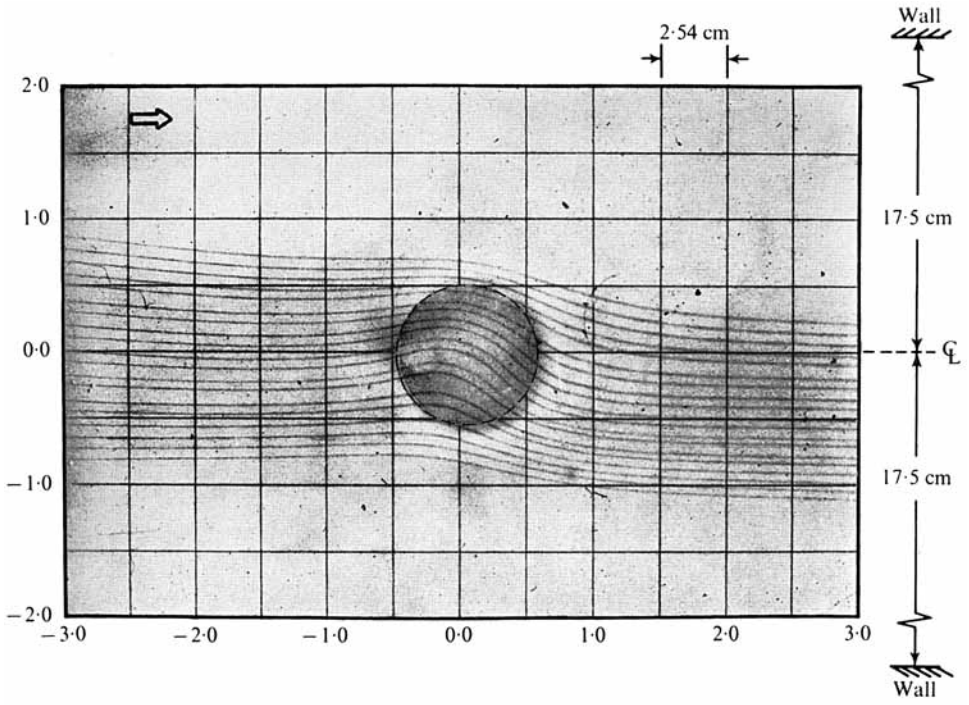

(*a*)

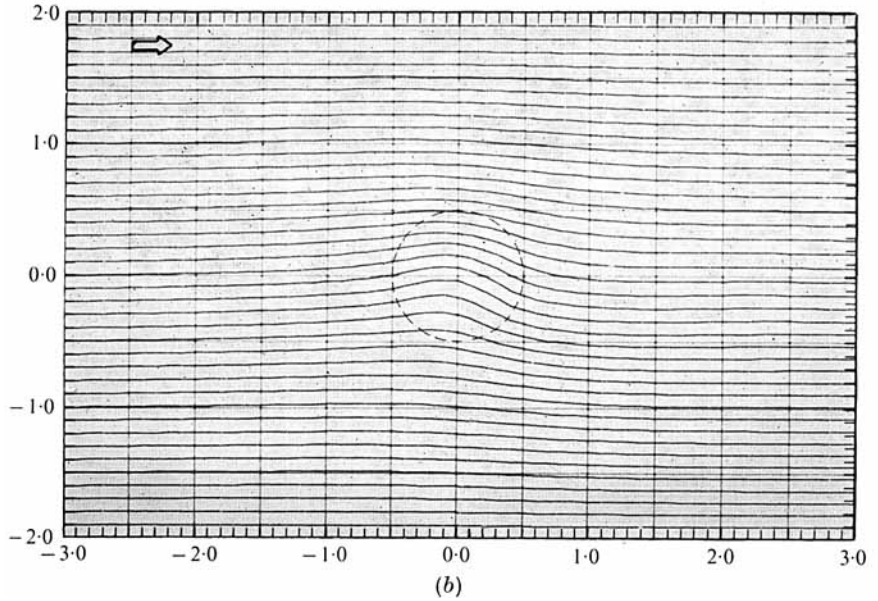

(*b*)

FIGURE 8. Streamline patterns for a conical topography, $Ro = 4{\cdot}0 \times 10^{-2}$, $E = 3{\cdot}0 \times 10^{-4}$, $H/D = 0{\cdot}375$ and $h/D = 6{\cdot}25 \times 10^{-2}$. (*a*) Experiment. (*b*) Numerical solution.

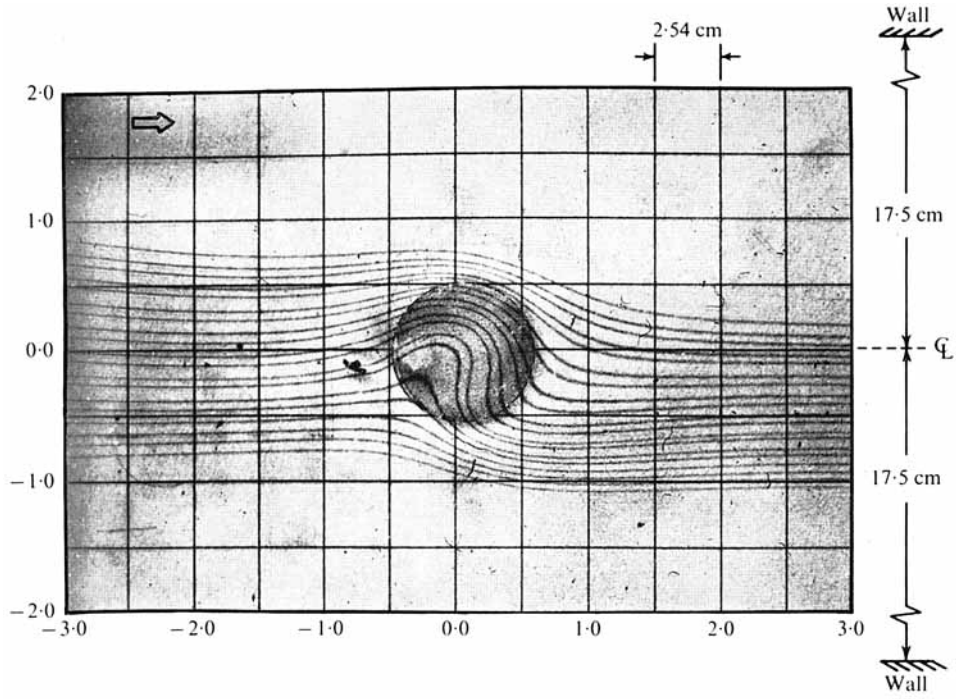

(*a*)

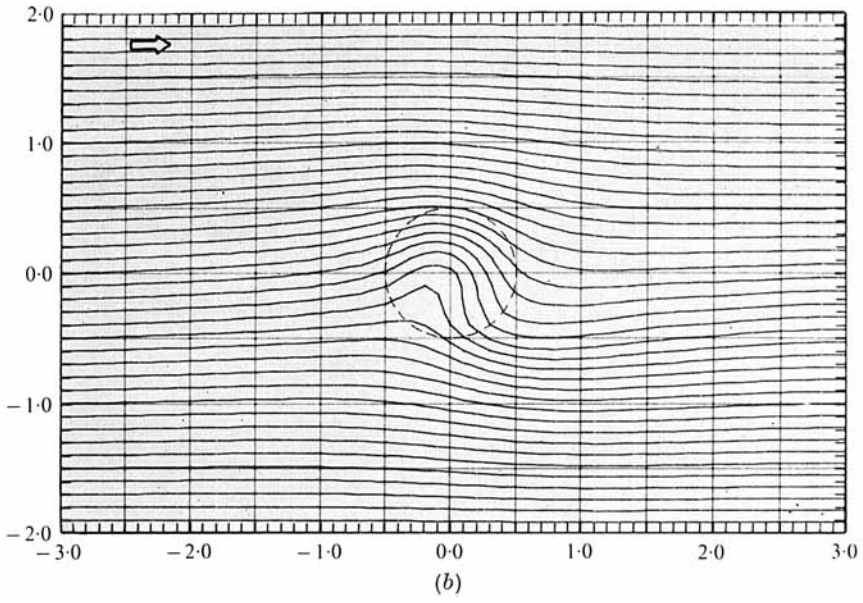

(*b*)

FIGURE 9. Same as figure 8 except for $E = 1{\cdot}0 \times 10^{-4}$.
(*a*) Experiment. (*b*) Numerical solution.

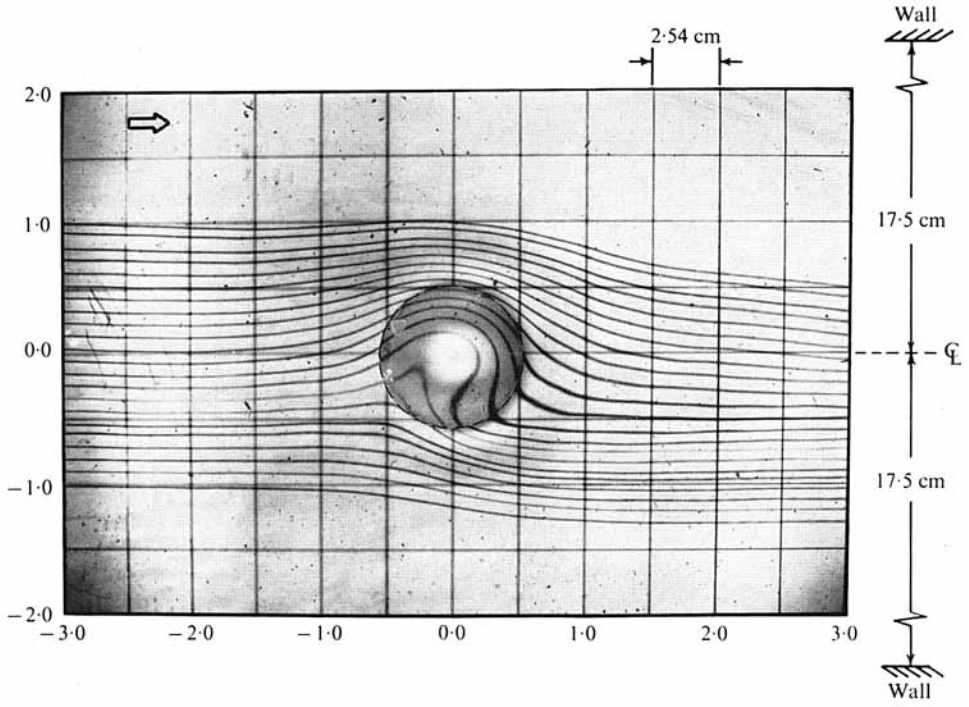

(*a*)

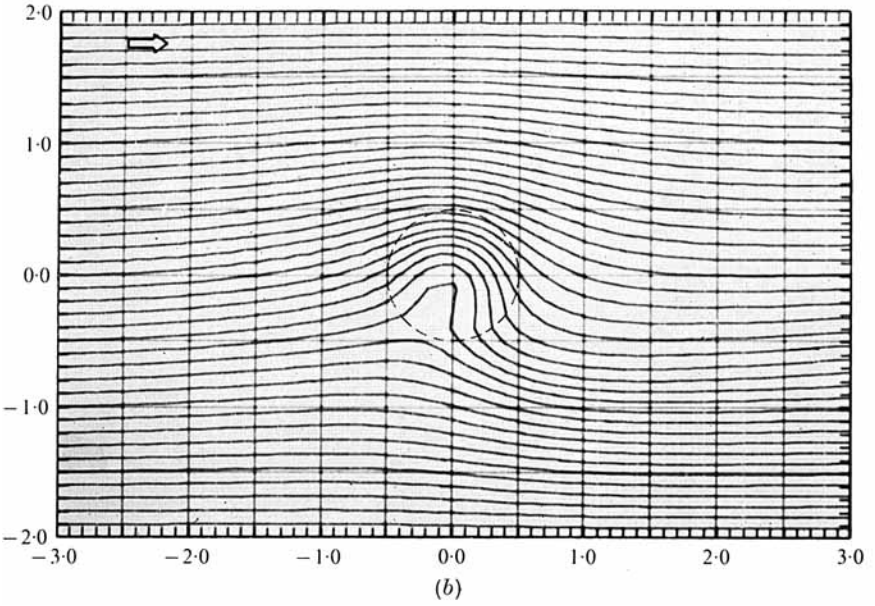

(*b*)

FIGURE 10. Streamline patterns for a conical topography of large amplitude. $Ro = 6{\cdot}0 \times 10^{-2}$, $E = 4{\cdot}0 \times 10^{-4}$, $H/D = 0{\cdot}375$ and $h/D = 0{\cdot}3$. (*a*) Experiment. (*b*) Numerical solution.